LETTER

https://doi.org/10.1038/s41586-018-0443-1

The gravitationally unstable gas disk of a starburst galaxy 12 billion years ago

K. Tadaki[1]*, D. Iono[1,2], M. S. Yun[3], I. Aretxaga[4], B. Hatsukade[5], D. H. Hughes[4], S. Ikarashi[6], T. Izumi[1], R. Kawabe[1,2,7], K. Kohno[5,8], M. Lee[1,9], Y. Matsuda[1,2], K. Nakanishi[1,2], T. Saito[10], Y. Tamura[9], J. Ueda[1], H. Umehata[5,11], G. W. Wilson[3], T. Michiyama[1,2], M. Ando[1,2] & P. Kamieneski[3]

Galaxies in the early Universe that are bright at submillimetre wavelengths (submillimetre-bright galaxies) are forming stars at a rate roughly 1,000 times higher than the Milky Way. A large fraction of the new stars form in the central kiloparsec of the galaxy[1–3], a region that is comparable in size to the massive, quiescent galaxies found at the peak of cosmic star-formation history[4] and the cores of present-day giant elliptical galaxies. The physical and kinematic properties inside these compact starburst cores are poorly understood because probing them at relevant spatial scales requires extremely high angular resolution. Here we report observations with a linear resolution of 550 parsecs of gas and dust in an unlensed, submillimetre-bright galaxy at a redshift of $z = 4.3$, when the Universe was less than two billion years old. We resolve the spatial and kinematic structure of the molecular gas inside the heavily dust-obscured core and show that the underlying gas disk is clumpy and rotationally supported (that is, its rotation velocity is larger than the velocity dispersion). Our analysis of the molecular gas mass per unit area suggests that the starburst disk is gravitationally unstable, which implies that the self-gravity of the gas is stronger than the differential rotation of the disk and the internal pressure due to stellar-radiation feedback. As a result of the gravitational instability in the disk, the molecular gas would be consumed by star formation on a timescale of 100 million years, which is comparable to gas depletion times in merging starburst galaxies[5].

Since the discovery of submillimetre-bright galaxies (SMGs) at high redshift[6,7] two decades ago, studies of their global physical properties, such as redshift, gas mass and kinematics, have helped us to understand the origin of the extreme starburst[8–12]. With the same goal in mind, we obtained observations of the CO $J = 4$–3 emission line in the $z = 4.3$ SMG COSMOS-AzTEC-1 (hereafter 'AzTEC-1') with the highest angular resolution yet achieved using the Atacama Large Millimeter/submillimetre Array (ALMA). AzTEC-1 is one of the brightest unlensed objects of this type, with an extraordinarily high star formation rate of $1{,}186^{+36}_{-291} M_{\odot}\,\mathrm{yr}^{-1}$ (where $M_{\odot}$ is the mass of the Sun) and a compact starburst with a half-light radius of $R_{1/2} = 1.1 \pm 0.1$ kpc measured in the 860-μm continuum[13]. These ALMA observations resolve the CO emission at a resolution of 0.08″ (550 pc in the physical scale) to reveal the morphology and kinematics of molecular gas within the central 2 kpc of the galaxy. In Fig. 1 we show ALMA maps of the CO line and the dust continuum at 3.2 mm and 860 μm, the velocity field and the velocity dispersion. The spatial distributions of the CO line and the 3.2-mm continuum emission independently confirm the existence of two off-centre clumps (clump 2 and clump 3), which were first detected in the 860-μm continuum[13]. Previous lower-resolution (0.15″–0.3″) observations[1–3,14] have found that SMGs and optically selected massive galaxies are associated with a very compact and dusty star-forming region with $R_{1/2} = 1$–2 kpc. However, our higher-resolution data demonstrate that the central structure of molecular gas and dust is more complicated than just a single, compact component. Such clumps of molecular gas are also seen in the central disk of the $z = 3$ gravitationally lensed star-forming galaxy SDP 81[15,16].

In addition, we made a 0.06″-resolution CO cube and a 0.05″-resolution 860-μm continuum image with different visibility weightings, to filter out the underlying disk emission and to highlight the clump structures (Methods). The higher-resolution velocity-integrated CO maps show that the clumps of molecular gas are aligned with the dusty star-forming clumps in the 860-μm continuum (Fig. 2). They are the second- and third-brightest clumps of 11 clumps identified previously[13] at 860 μm. Because the brightest clump is very close to the nucleus, it is difficult to isolate even at a resolution of 0.06″. Other faint star-forming clumps are not detected in the CO data, probably owing to poor sensitivity.

We fit the CO spectra of the clumps with a single Gaussian to derive full-width at half-maximum (FWHM) line widths of 250 ± 50 km s^{-1} and 240 ± 50 km s^{-1} for clumps 2 and 3, respectively. These line widths are one or two orders of magnitude larger than those of giant molecular clouds in nearby galaxies[17]. The integrated CO line flux is $S_{\mathrm{CO}}\mathrm{d}v = 0.056 \pm 0.009$ Jy km s^{-1} for clump 2 and $S_{\mathrm{CO}}\mathrm{d}v = 0.042 \pm 0.007$ Jy km s^{-1} for clump 3, indicating that each clump contains only a few per cent of the total gas mass. (Here and elsewhere, the errors quoted correspond to one standard deviation.) Adopting a CO-to-H_2 conversion factor of $\alpha_{\mathrm{CO}} = 0.8 M_{\odot}$ (K km s^{-1} pc^2)$^{-1}$ and a CO excitation of $R_{41} = 0.91$, we derive gas masses of $M_{\mathrm{CO,gas}} = (2.2 \pm 0.3) \times 10^9 M_{\odot}$ and $M_{\mathrm{CO,gas}} = (1.7 \pm 0.3) \times 10^9 M_{\odot}$ for the two gas clumps (Methods), which are 3–5 orders of magnitude larger than the virial mass of giant molecular clouds. Therefore, these giant clumps are completely different from giant molecular clouds in nearby galaxies.

We fit the CO cube with a dynamical model to derive the kinematic properties of the CO-emitting gas. The observed velocity field is well characterized by a rotating disk with $R_{1/2} = 1.05 \pm 0.02$ kpc, a deprojected maximum rotation speed of $v_{\mathrm{max}} = 227^{+5}_{-6}$ km s^{-1} and a local velocity dispersion of $\sigma_0 = 74 \pm 1$ km s^{-1}. The starburst gas disk is rotation-dominated with a ratio of rotation velocity to velocity dispersion of $v_{\mathrm{max}}/\sigma_0 = 3.1 \pm 0.1$. In the local Universe, 80% of massive early-type galaxies with stellar masses of $\log(M_{\mathrm{star}}/M_{\odot}) > 11.8$ exhibit dispersion-dominated stellar kinematics with $v_{\mathrm{max}}/\sigma_0 < 1$, whereas less-massive ones are rotation-dominated[18,19]. Given the large stellar mass of $M_{\mathrm{star}} = (9.9^{+0.4}_{-2.6}) \times 10^{10} M_{\odot}$ (Methods), AzTEC-1 is near the massive end at $z = 4$ and might eventually evolve to become one of the most massive early-type galaxies at $z = 0$. If molecular gas and stars share the same kinematics, then the observed properties of the rotating disk suggest that the most massive galaxies do not lose much of their angular momentum during the formation phase; instead, they lose it during the subsequent evolution phase, such as during major mergers[20].

[1]National Astronomical Observatory of Japan, Tokyo, Japan. [2]SOKENDAI (The Graduate University for Advanced Studies), Tokyo, Japan. [3]Department of Astronomy, University of Massachusetts, Amherst, MA, USA. [4]Instituto Nacional de Astrofisica, Opticay Electronica (INAOE), Puebla, Mexico. [5]Institute of Astronomy, Graduate School of Science, The University of Tokyo, Tokyo, Japan. [6]Kapteyn Astronomical Institute, University of Groningen, Groningen, The Netherlands. [7]Department of Astronomy, The University of Tokyo, Tokyo, Japan. [8]Research Center for the Early Universe, The University of Tokyo, Tokyo, Japan. [9]Division of Particle and Astrophysical Science, Nagoya University, Nagoya, Japan. [10]Max-Planck-Institute for Astronomy, Heidelberg, Germany. [11]RIKEN Cluster for Pioneering Research, Saitama, Japan. *e-mail: tadaki.ken@nao.ac.jp

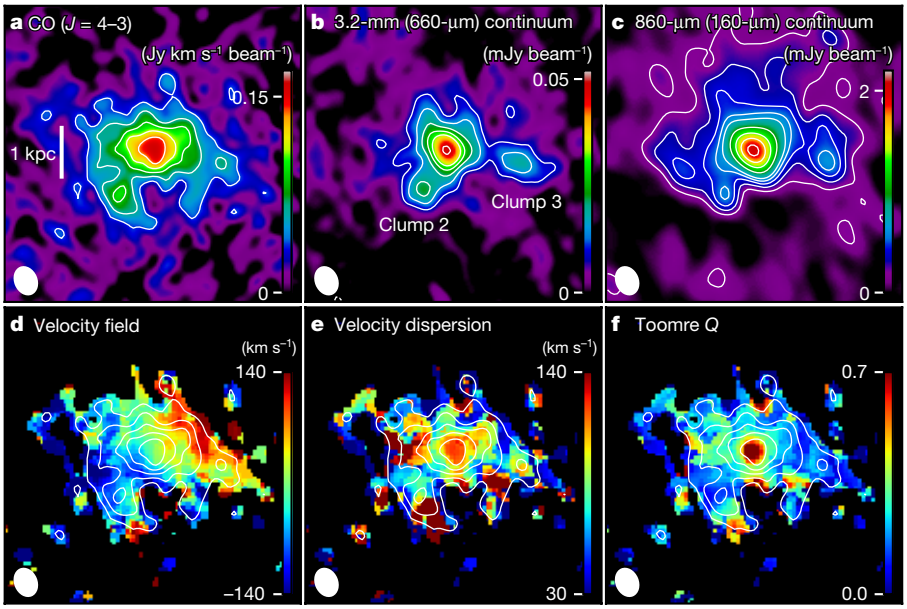

Fig. 1 | CO morphology and kinematics of AzTEC-1. a–f, ALMA maps of the CO ($J = 4–3$) line (**a**), 3.2-mm continuum (**b**) and 860-μm continuum (**c**), velocity field (**d**), velocity dispersion (**e**) and Toomre Q parameter (**f**). The numbers in parentheses in **b** and **c** refer to the rest-frame wavelength. The angular resolution (indicated by the white ellipses) is $0.093'' \times 0.072''$ in all cases. The CO line is integrated in the velocity range -315 km s^{-1} to $+315$ km s^{-1}. Contours in **a**–**c** are plotted every 2σ from 3σ to 11σ and every 5σ from 11σ, where 1σ is the noise level; the contours in **a** are also overplotted in **d**–**f**.

Until recently, clumpy rotating disks at high redshift have been discovered from observations of ionized gas[21]. Now, higher-resolution observations of molecular gas using ALMA can be used similarly. Observational and numerical studies show that giant clumps are spawned by gravitational instability in the outskirts of gas-rich disks and migrate inward by dynamical friction[22,23]. Using the ALMA maps of the CO line intensity and velocity dispersion without any correction for beam smearing (Fig. 1), we compute the local Toomre Q parameter, which describes the balance between self-gravity of molecular gas and turbulent pressure by stellar radiation and other sources. A thick, rotating disk can become unstable against local axisymmetric perturbations[24] if $Q < Q_{cri} = 0.7$. The local Q values that we measured are less than Q_{cri} over the entire disk, indicating that the gas disk should fragment and collapse through gravitational instability in the inter-clump

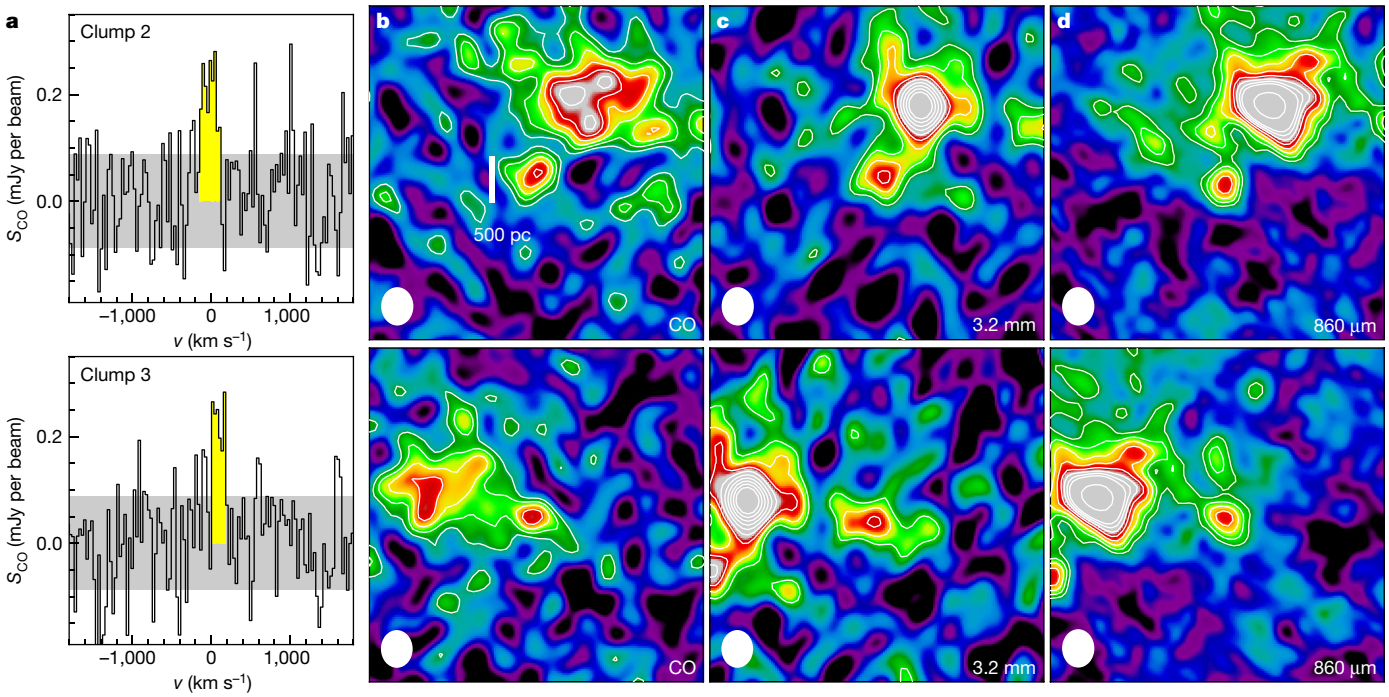

Fig. 2 | Spectra and maps of the two large clumps. a, For Clump 2 (top) and clump 3 (bottom), CO spectra are extracted from the Briggs-weighted cube with an angular resolution of $0.069'' \times 0.058''$. The grey shaded region indicates the standard deviation of the noise spectra. **b**–**d**, ALMA maps of the CO line (**b**), 3.2-mm continuum (**c**) and 860-μm continuum (**d**) for the two clumps. The CO flux densities are integrated over the velocity range indicated by the yellow shaded regions in **a**. White filled circles represent the angular resolution of each map. The contours are plotted every 1σ from 2σ in **b** and **c** and from 4σ in **d**, and at every 5σ from 10σ.

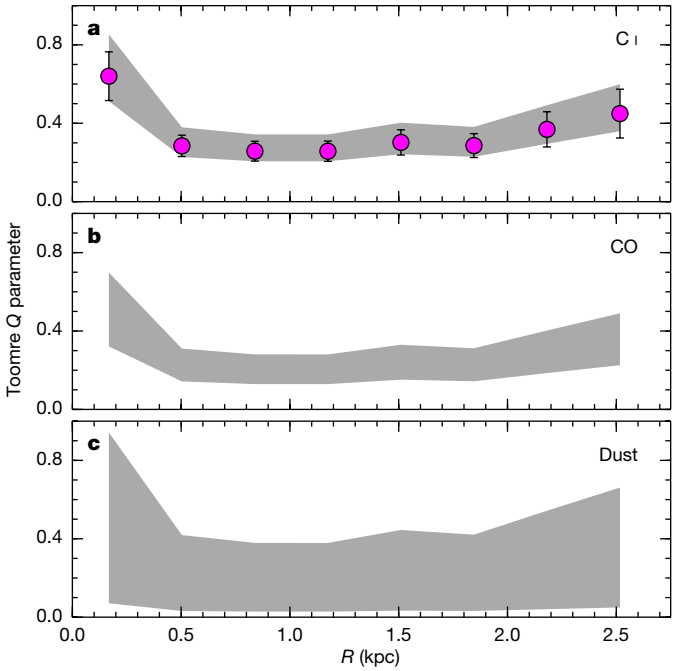

Fig. 3 | Radially averaged Toomre *Q* parameter. a, Magenta circles show the *Q* values computed using the C I-based gas mass. We adopt a carbon abundance relative to molecular hydrogen of $X_{\rm C\,I} = 4 \times 10^{-5}$. The error bars include the uncertainties of the C I excitation temperature and the kinematic parameters as well as the measurement errors of the CO flux (Methods). The grey shaded region indicates the effect of different carbon abundances, $X_{\rm CI} = (3–5) \times 10^{-5}$. **b**, **c**, We also compute the *Q* values using the CO-based (**b**) and dust-based (**c**) gas mass. The grey shaded regions illustrate the effect of changing assumptions of the ratio of the luminosities of the CO ($J = 4–3$) and CO ($J = 1–0$) lines, $R_{41} = 0.46–1.0$ (**b**), and of the dust-to-gas mass ratio, $\delta_{\rm GDR} = 44–589$ (**c**). *R* is the radial distance from the centre of the galaxy.

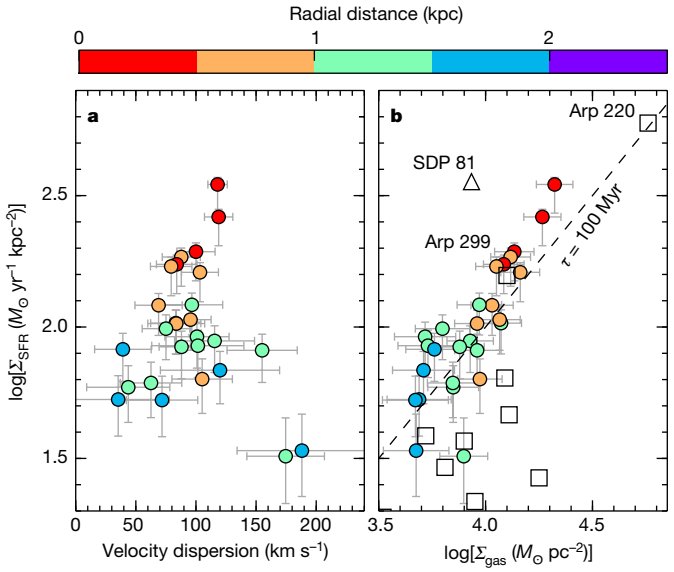

Fig. 4 | Pixel-to-pixel variations in the physical properties. a, **b**, The local velocity dispersion, gas mass per unit area $\Sigma_{\rm gas}$, and star-formation rate per unit area $\Sigma_{\rm SFR}$ are computed in a beam area of 0.344 kpc^2. The colour coding indicates the radial distance from the centre of the galaxy. Open squares and an open triangle show the galaxy-averaged values in nearby starburst galaxies[5] and the resolved value in a $z = 3$ gravitationally lensed galaxy[16], respectively. The error bars reflect the overall uncertainty, including the measurement uncertainties in the velocity dispersion, the 860-μm continuum flux and the CO line flux in each pixel, and the systematic uncertainties in the total star-formation rate and the total gas mass.

regions. On the other hand, $Q < Q_{\rm cri}$ at the clump locations means that the gas is gravitationally bound rather than gravitationally unstable. We also derive radially averaged *Q* parameters using the best-fit kinematic parameters with corrections for beam smearing and inclination. Here, the uncertainties in *Q* arise mainly from measurements of gas mass. We tackle this issue by determining three independent estimates of gas mass, from the C I ($J = 2–1$), CO ($J = 4–3$) and dust continuum data. All three methods indicate that $Q < 1$ is in the central 2.5 kpc of the galaxy, even after allowing for some variations in carbon abundance, CO excitation and the gas-to-dust mass ratio (Fig. 3).

In the current framework of galaxy evolution, galaxies self-regulate star formation with a marginally unstable disk[25,26]. If a galactic disk is unstable with $Q < Q_{\rm cri}$, intense stellar radiation temporarily boosts turbulent pressure and heats the disk until $Q > Q_{\rm cri}$. Once the disk is stable, star formation becomes inefficient, leading to a drop in turbulent pressure. On the other hand, gas accretion may increase the gas mass per unit area in the disk, and when the increased self-gravity of the gas overcomes the decreased pressure the disk becomes unstable again. Thus, galaxy disks are kept marginally unstable with $Q \approx Q_{\rm cri}$. In AzTEC-1, stellar radiation pressure is unlikely to support the self-gravity of gas, resulting in small *Q* values across the entire disk. The local velocity dispersion increases only slightly as the star-formation rate per unit area increases (Fig. 4), which suggests that stellar feedback by intense star formation does not control the velocity dispersion in the molecular gas in this case. We also find that the velocity dispersion of $\sigma \approx 100$ km s^{-1} in the two clumps is not much higher than in the rest of the disk. Our results imply that star-forming clumps are stable and not disrupted by radiative feedback. On the other hand, there is a strong correlation between the molecular gas mass per unit area ($\Sigma_{\rm gas}$) and the star-formation rate per unit area ($\Sigma_{\rm SFR}$), fitted by the linear relation $\log[\Sigma_{\rm SFR}/(M_\odot\,{\rm yr}^{-1}\,{\rm kpc}^{-2})] = (1.4 \pm 0.2) \times \log[\Sigma_{\rm gas}/(M_\odot\,{\rm pc}^{-2})] + (-3.6 \pm 0.7)$. The gas mass per unit area derived for AzTEC-1 is extremely high, with $\log[\Sigma_{\rm gas}/(M_\odot\,{\rm pc}^{-2})] = 3.8–4.4$, similar in magnitude to that seen in nearby starburst galaxies[5]. The implied gravitational instability is a consequence of the strong concentration of molecular gas.

In such a gravitationally unstable gas disk, molecular clouds are expected to be converted into stars efficiently. The gas depletion time in the starburst disk, defined as the gas mass divided by the star-formation rate, is comparable to the galaxy-averaged gas depletion time in nearby starburst galaxies (Fig. 4). The molecular gas reservoir of AzTEC-1 will be consumed by star formation within 100 million years, a timescale that is roughly ten times shorter than the gas depletion time in star-forming galaxies at $z = 1–3$[27] and comparable to the gas depletion times in nearby merging galaxies such as Arp 220 and Arp 299[5] and the $z = 3$ lensed star-forming galaxy SDP 81[16]. An extreme starburst at high redshift may occur over a very short timescale, resulting in episodic bright periods in the submillimetre band. Otherwise, it requires new gas flowing into the central region to maintain the current level of star-formation activity.

It is still uncertain how a large amount of molecular gas is concentrated in the central 2 kpc of the galaxy. A gas-rich major merger is the most straightforward scenario, because several numerical simulations have successfully reproduced the physical properties of SMGs[28], including the compact gas distribution and the enhanced star-forming activity. We cannot necessarily reject the major merger scenario for rotating disk because nearby merger remnants frequently host a rotationally supported structure[29]; however, we do not have direct evidence for a major merger in AzTEC-1. In addition to a past gas-rich major merger, multiple gas-rich minor mergers or clumpy gas streams could also lead to gas transport to the central 2 kpc[30]. Isolated galaxies require a non-axisymmetric structure such as spiral arms or a bar to remove the angular momentum and transport a large amount of gas into the galaxy centre. AzTEC-1 does not have such a non-axisymmetric structure. To determine the roles of major mergers in extreme starbursts, we need to investigate morphological and kinematic structures in a large sample of

high-redshift SMGs using high-resolution (less than 0.1″) and sensitive observations with ALMA.

Online content

Any Methods, including any statements of data availability and Nature Research reporting summaries, along with any additional references and Source Data files, are available in the online version of the paper at https://doi.org/10.1038/s41586-018-0443-1.

Received: 12 April 2018; Accepted: 29 June 2018;
Published online 29 August 2018.

1. Swinbank, A. M. et al. Intense star formation within resolved compact regions in a galaxy at $z = 2.3$. *Nature* **464**, 733–736 (2010).
2. Ikarashi, S. et al. Compact starbursts in $z \sim 3$–6 submillimeter galaxies revealed by ALMA. *Astrophys. J.* **810**, 133 (2015).
3. Simpson, J. M. et al. The SCUBA-2 cosmology legacy survey: ALMA resolves the rest-frame far-infrared emission of sub-millimeter galaxies. *Astrophys. J.* **799**, 81 (2015).
4. van Dokkum, P. et al. Forming compact massive galaxies. *Astrophys. J.* **813**, 23 (2015).
5. Kennicutt, R. C. Jr. The global Schmidt law in star-forming galaxies. *Astrophys. J.* **498**, 541–552 (1998).
6. Hughes, D. H. et al. High-redshift star formation in the Hubble Deep Field revealed by a submillimetre-wavelength survey. *Nature* **394**, 241–247 (1998).
7. Barger, A. J. et al. Submillimetre-wavelength detection of dusty star-forming galaxies at high redshift. *Nature* **394**, 248–251 (1998).
8. Chapman, S. C. et al. A redshift survey of the submillimeter galaxy population. *Astrophys. J.* **622**, 772–796 (2005).
9. Bothwell, M. S. et al. A survey of molecular gas in luminous sub-millimetre galaxies. *Mon. Not. R. Astron. Soc.* **429**, 3047–3067 (2013).
10. Ivison, R. J. et al. Herschel-ATLAS: a binary HyLIRG pinpointing a cluster of starbursting protoellipticals. *Astrophys. J.* **772**, 137 (2013).
11. Tacconi, L. J. et al. Submillimeter galaxies at $z \sim 2$: evidence for major mergers and constraints on lifetimes, IMF, and CO-H_2 conversion factor. *Astrophys. J.* **680**, 246–262 (2008).
12. Hodge, J. A. et al. Evidence for a clumpy, rotating gas disk in a submillimeter galaxy at $z = 4$. *Astrophys. J.* **760**, 11 (2012).
13. Iono, D. et al. Clumpy and extended starbursts in the brightest unlensed submillimeter galaxies. *Astrophys. J.* **829**, L10 (2016).
14. Tadaki, K.-i. et al. Bulge-forming galaxies with an extended rotating disk at $z \sim 2$. *Astrophys. J.* **834**, 135 (2017).
15. Swinbank, A. M. et al. ALMA resolves the properties of star-forming regions in a dense gas disk at $z \sim 3$. *Astrophys. J.* **806**, L17 (2015).
16. Sharda, P. et al. Testing star formation laws in a starburst galaxy at redshift 3 resolved with ALMA. *Mon. Not. R. Astron. Soc.* **477**, 4380–4390 (2018).
17. Bolatto, A. D. et al. The resolved properties of extragalactic giant molecular clouds. *Astrophys. J.* **686**, 948–965 (2008).
18. Cappellari, M. Structure and kinematics of early-type galaxies from integral field spectroscopy. *Annu. Rev. Astron. Astrophys.* **54**, 597–665 (2016).
19. Veale, M. et al. The MASSIVE survey – V. Spatially resolved stellar angular momentum, velocity dispersion, and higher moments of the 41 most massive local early-type galaxies. *Mon. Not. R. Astron. Soc.* **464**, 356–384 (2017).
20. Naab, T. et al. The ATLAS^{3D} project – XXV. Two-dimensional kinematic analysis of simulated galaxies and the cosmological origin of fast and slow rotators. *Mon. Not. R. Astron. Soc.* **444**, 3357–3387 (2014).
21. Genzel, R. et al. The Sins survey of $z \sim 2$ galaxy kinematics: properties of the giant star-forming clumps. *Astrophys. J.* **733**, 101 (2011).
22. Bournaud, F. et al. The long lives of giant clumps and the birth of outflows in gas-rich galaxies at high-redshift. *Astrophys. J.* **780**, 57–75 (2014).
23. Mandelker, N. et al. The population of giant clumps in simulated high-z galaxies: in situ and ex situ migration and survival. *Mon. Not. R. Astron. Soc.* **443**, 3675–3702 (2014).
24. Genzel, R. et al. The SINS/zC-SINF survey of $z \sim 2$ galaxy kinematics: evidence for gravitational quenching. *Astrophys. J.* **785**, 75 (2014).
25. Thompson, T. et al. Radiation pressure-supported starburst disks and active galactic nucleus fueling. *Astrophys. J.* **630**, 167–185 (2005).
26. Cacciato, M. et al. Evolution of violent gravitational disc instability in galaxies: late stabilization by transition from gas to stellar dominance. *Mon. Not. R. Astron. Soc.* **421**, 818–831 (2012).
27. Tacconi, L. J. et al. Phibss: molecular gas content and scaling relations in $z \sim 1$–3 massive, main-sequence star-forming galaxies. *Astrophys. J.* **768**, 74 (2013).
28. Narayanan, D. et al. The star-forming molecular gas in high-redshift submillimetre galaxies. *Mon. Not. R. Astron. Soc.* **400**, 1919–1935 (2009).
29. Ueda, J. et al. Cold molecular gas in merger remnants. I. Formation of molecular gas disks. *Astrophys. J. Suppl. Ser.* **214**, 1 (2014).
30. Dekel, A. et al. Cold streams in early massive hot haloes as the main mode of galaxy formation. *Nature* **457**, 451–454 (2009).

Acknowledgements We thank J. Baba for discussions about a gravitational instability in SMGs. This work was supported by JSPS KAKENHI JP17J04449. We thank the ALMA staff and in particular the EA-ARC staff for their support. This research has made use of data from ALMA and HerMES project (http://hermes.sussex.ac.uk/). ALMA is a partnership of ESO (representing its member states), NSF (USA) and NINS (Japan), together with NRC (Canada), MOST and ASIAA (Taiwan), and KASI (South Korea), in cooperation with the Republic of Chile. The Joint ALMA Observatory is operated by ESO, AUI/NRAO and NAOJ. HerMES is a Herschel Key Programme utilizing Guaranteed Time from the SPIRE instrument team, ESAC scientists and a mission scientist. Data analysis was in part carried out on the common-use data analysis computer system at the Astronomy Data Center (ADC) of the National Astronomical Observatory of Japan.

Reviewer information *Nature* thanks F. Bournaud and the other anonymous reviewer(s) for their contribution to the peer review of this work.

Author contributions K.T. led the project and reduced the ALMA data. K.T. and D.I. wrote the manuscript. M.S.Y. reduced the Large Millimeter Telescope data and edited the final manuscript. Other authors contributed to the interpretation and commented on the ALMA proposal and the paper.

Competing interests The authors declare no competing interests.

Additional information
Extended data is available for this paper at https://doi.org/10.1038/s41586-018-0443-1.
Supplementary information is available for this paper at https://doi.org/10.1038/s41586-018-0443-1.
Reprints and permissions information is available at http://www.nature.com/reprints.
Correspondence and requests for materials should be addressed to K.T.
Publisher's note: Springer Nature remains neutral with regard to jurisdictional claims in published maps and institutional affiliations.

METHODS

Sample. AzTEC-1 was first discovered as one of the brightest sources in a 1.1-mm continuum survey of the COSMOS field obtained using the AzTEC bolometer camera on the James Clerk Maxwell Telescope (JCMT)[31]. Follow-up observations with the Redshift Search Receiver on the Large Millimeter Telescope (LMT) detected CO (4–3) and CO (5–4) lines and yielded a spectroscopic redshift of $z = 4.342$, which is also confirmed by the detection of the [C II] line using the Submillimetre Array[32]. Previous ALMA observations of the 860-μm continuum emission at 0.02″ resolution revealed that AzTEC-1 is composed of a compact core, an extended disk and multiple 200-pc clumps within the disk[13]. The half-light radius for the 860-μm continuum emission is $R_{1/2} = 1.1 \pm 0.1$ kpc. The rest-frame ultraviolet continuum emission is not resolved even by Hubble Space Telescope (HST)/WFC3 imaging, which is also suggestive of compact emission with $R_{1/2} < 2.6$ kpc[33]. In this work, the Chabrier initial mass function[34] and the following cosmological parameters are assumed: present-day Hubble parameter $H_0 = 70$ km s^{-1} Mpc^{-1}, matter-density parameter $\Omega_M = 0.3$ and density parameter for the cosmological constant $\Omega_\Lambda = 0.7$. At $z = 4.342$, an angular scale of 0.1″ corresponds to a physical scale of 670 pc.

Observations. In AzTEC-1, we carried out observations of the CO (4–3) emission line at the rest-frame frequency of 461.040 GHz (86.309 GHz in the observed frame), with ALMA band-3 receivers covering the frequency range of 85.4–89.1 GHz and 97.5–101.2 GHz in two array configurations and baseline lengths of 41 m to 16.2 km. The shortest 5th-percentile baseline is 600 m, corresponding to the maximum recoverable scale of 1.15″ at 86.3 GHz. The observations were executed on 2017 October (C43-10 array configuration) and November (C43-8). On-source time was 5.8 h and 1.2 h, respectively. The total observing time including calibration and overhead was 14 h. We used the Common Astronomy Software Application (CASA) package[35] for data calibration. We first estimated the continuum flux density in the frequency range excluding 86.1–86.5 GHz, and then subtracted it from the data in the visibility plane using the CASA/*uvcontsub* task. We used the CASA/*tclean* task with natural weighting to make a cube with a velocity width of 30 km s^{-1}. The resultant angular resolution and the noise level are 0.093″ × 0.072″ (624 pc × 483 pc in physical scale) and $1\sigma = 78$ μJy per 30 km s^{-1}, respectively. We cleaned down to the 2σ noise level in a circular mask with a radius of 0.4″. We also made a high-resolution cube of the CO (4–3) line with a Briggs weighting (robust parameter of +0.5). The angular resolution is then 0.069″ × 0.058″ (470 pc × 390 pc) and the noise level is $1\sigma = 87$ μJy per 30 km s^{-1}. To show the significance of the clump detection in AzTEC-1, we also made a 0.055″ × 0.042″ map of the 860-μm continuum emission using archival ALMA data[13]. We adopted a taper of 0.03″ in the visibility plane, resulting in a standard deviation of 47 μJy. We use the high-resolution cube and map only for studying the clump properties in Fig. 2.

Extended Data Fig. 1 shows the galaxy-integrated CO (4–3) spectrum extracted within an aperture of 0.8″ centred on AzTEC-1. The Gaussian line width derived is 305 ± 17 km s^{-1} (FWHM). We made the CO moment maps of velocity-integrated intensity, velocity field and velocity dispersion in the velocity range between −315 km s^{-1} and +315 km s^{-1} using the CASA/*immoments* task. A 2σ masking threshold was adopted when creating the velocity field and velocity dispersion maps. The total CO line flux measured is $S_{CO}\Delta v = 1.84 \pm 0.17$ Jy km s^{-1} with 0.8″ aperture photometry in the velocity-integrated intensity map. The uncertainty in the CO line flux measurement is estimated by placing 300 random apertures in the same map. The CO line flux and the velocity width measured by the LMT are[32] $S_{CO}\Delta v = 1.75 \pm 0.24$ Jy km s^{-1} and $\Delta v = 380$ km s^{-1}, in good agreement with the ALMA-derived flux of $S_{CO}\Delta v = 1.60 \pm 0.13$ Jy km s^{-1} with $\Delta v = 390$ km s^{-1}.

We also created two 3.2-mm line-free continuum maps with the same angular resolution as the CO (4–3) cubes by excluding the CO frequency range. The root-mean-square noise is 3.0 μJy per beam in the 0.093″ × 0.072″ map and 3.3 μJy per beam in the 0.069″ × 0.058″ map. We derived a total flux density of $S_{3.2mm} = 273 \pm 41$ μJy with an aperture of 0.8″, consistent with the 3-mm continuum flux density of $S_{3mm} = 300 \pm 40$ μJy from Plateau de Bure interferometer observations with a 6″ beam[36].

We made follow-up observations of the C I (1–0) line at 92.134 GHz in the observed frame and the C I (2–1) line at 151.511 GHz with ALMA band-3 and band-4 receivers in March 2018. We reduced the data in a similar way as for the CO (4–3) data and created a cube with a spectral resolution of 30 km s^{-1} and a map of the 2.1-mm continuum with a Briggs weighting (robust parameter of +0.5). The angular resolution is 1.7″ × 1.1″ in the C I (1–0) map and 0.8″ × 0.7″ in the C I (2–1) map. The noise level is $1\sigma = 0.49$ mJy in each 30 km s^{-1} channel in the C I (1–0) cube, $1\sigma = 0.38$ mJy in the C I (2–1) cube and $1\sigma = 20$ μJy in the 2.1-mm continuum map. For the flux measurements of the two C I lines, we integrated the line flux density in the same velocity range as for the CO (4–3) line. We also made a natural weighted C I (2–1) map with the same angular resolution as for the C I (1–0) map using the CASA/*imsmooth* task, which is used to obtain a C I (1–0)/C I (2–1) line ratio. In Extended Data Fig. 1 and Extended Data Table 1, we show the line spectra and tabulate the measured line fluxes and luminosities. The 2.1-mm continuum flux density is $S_{2.1mm} = 989 \pm 20$ μJy. We also detected the CO (7–6) emission line at 151.007 GHz, but do not discuss this information here.

Global SED properties of AzTEC-1. We collected the photometric data for AzTEC-1 from the latest multi-wavelength catalogues (Subaru[37], VISTA[37], Spitzer[37], Hershel[38,39] and VLA[40]). After excluding marginal detections below 5σ and adding our ALMA photometry at 860 μm, 2.1 mm and 3.2 mm, we constrained the global spectral energy distribution (SED) from optical to radio (Extended Data Fig. 2). To account for possible zero-point offsets, we added a systematic uncertainty of 0.1 mag to the flux errors in the optical and near-infrared bands. Using the MAGPHYS code[41,42], we fitted the observed SED to stellar population synthesis models[43], taking into account dust attenuation and dust emission in a physically consistent way. The best-fitting SED model indicates that AzTEC-1 is a massive, star-forming galaxy with a stellar mass of $M_{star} = (9.9^{+0.4}_{-2.6}) \times 10^{10} M_\odot$ and a star-formation rate of SFR $= 1{,}186^{+36}_{-291} M_\odot$ yr^{-1}. The dust emission is characterized by a total infrared luminosity of $L_{dust} = (1.9^{+0.0}_{-0.3}) \times 10^{13} L_\odot$, a dust mass of $M_{dust} = (1.1 \pm 0.2) \times 10^9 M_\odot$ and a dust temperature of $T_{dust} = 43^{+4}_{-2}$K. The uncertainties are based on the 2.5th–97.5th-percentile range of the probability distributions.

Gas mass. We derived two independent estimates the molecular gas mass for AzTEC-1 using the CO (4–3) line and [C I] line luminosities. For the gas-mass estimates based on the CO (4–3) luminosity, there are uncertainties about the CO excitation $R_{41} = L'_{CO(4-3)}/L'_{CO(1-0)}$ and the CO-to-H_2 conversion factor $\alpha_{CO} = M_{gas}/L'_{CO}$. Alternatively, the [C I] line is an independent, optically thin tracer of cold molecular gas mass in nearby and high-redshift galaxies[44–48], and having both [C I] line measurements provides useful constraints on the physical conditions of the emitting gas. First, we estimated an excitation temperature of $T_{ex} = 27.7 \pm 4.8$ K from the C I (1–0)/C I (2–1) line ratio of $R_{CI} = 0.52 \pm 0.13$ in the 1.7″ × 1.1″ resolution maps, using the relation[45] $T_{ex} = 38.8\ \mathrm{K}/\ln(2.11/R_{CI})$. Then, using the C I (2–1) line flux in the 0.8″ × 0.7″ map, we computed a neutral carbon mass of $M_{CI} = (1.7 \pm 0.3) \times 10^7 M_\odot$ from $M_{CI} = 4.566 \times 10^{-4} Q(T_{ex}) \times 1/5 \times \exp(62.5/T_{ex}) L'_{CI(2-1)}$, where $Q(T_{ex}) = 1 + 3\exp(-23.6/T_{ex}) + 5\exp(-62.5/T_{ex})$ is the partition function[45]. The uncertainty in the neutral carbon mass includes the error in the flux measurement and the uncertainty in the excitation temperature. The molecular gas mass derived from the [C I] line luminosity is $M_{CI,gas} = (7.2 \pm 1.3) \times 10^{10} M_\odot$, adopting carbon abundance of $X_{CI} = 4 \times 10^{-5}$, which is the average of the typical value of 3×10^{-5} in normal star-forming galaxies[44–48] and the elevated value of 5×10^{-5} in the central region of the local starburst galaxy M82[49]. The resulting gas-to-dust mass ratio $M_{CI,gas}/M_{dust} = 65 \pm 17$ is smaller than the average value of $\delta_{GDR} = 120 \pm 28$ in 18 nearby starburst galaxies[50], but is still in the 5th–95th-percentile range, $\delta_{GDR} = 44$–589. The CO (4–3) luminosity also gives a gas mass of $M_{CO,gas} = (6.6 \pm 0.6) \times 10^{10} \times \alpha_{CO}/0.8 \times (1.0/R_{41}) M_\odot$. If the CO (4–3) line is thermalized ($R_{41} = 1$) and the conversion factor of $\alpha_{CO} = 0.8 M_\odot$ (K km s^{-1} pc^2)$^{-1}$ is used[11,12,51,52], then the CO-based gas mass is similar to the C I-based gas mass. For consistency between C I and CO, we adopt a gas excitation of $R_{41} = 0.91$, which is larger than the average value for SMGs at high redshift ($R_{41} = 0.46$) and comparable with the average value for quasi-stellar objects ($R_{41} = 0.87$)[53]. Adopting $\alpha_{CO} = 4 M_\odot$ (K km s^{-1} pc^2)$^{-1}$, commonly used in normal star-forming galaxies[51], is not appropriate because the CO-based gas mass substantially exceeds the C I-based gas mass. Modelling suggests that CO emission in dense clumps is more highly excited, compared with the entire disk[54]. If the gas is thermalized with $R_{41} = 1$, then the gas mass of clumps can be 10% smaller.

SFR and gas mass per unit area. We obtained the total star-formation rate SFR_{total} and gas mass $M_{gas,total}$ in AzTEC-1 as mentioned above. Because the 860-μm (160 μm in the rest frame) continuum flux density $S_{860\mu m}$ traces star formation, we compute star-formation-rate surface densities in each pixel as $\Sigma_{SFR} = SFR_{total} \times (S_{860\mu m}/S_{860\mu m,total})/\Omega_{beam}$, where $S_{860\mu m,total} = 16.9 \pm 0.7$ mJy and Ω_{beam} is the effective beam area of 0.344 kpc^2. Here, we use the 860-μm continuum map with a pixel scale of 0.07″ to avoid oversampling, although the original pixel scale is 0.01″. The uncertainties of Σ_{SFR} include errors in the flux measurements of $S_{860\mu m}$ and $S_{860\mu m,total}$ and systematic errors in the SED modelling. In a similar way, using the CO (4–3) map, we derive gas mass surface densities as $\Sigma_{gas} = M_{gas,total} \times (S_{CO}\Delta v/S_{CO,total}\Delta v)/\Omega_{beam}$.

Disk modelling and dynamical mass. We fit the natural-weighted CO cube with dynamical models of a disk galaxy using the GalPaK^{3D} code[55]. We adopt a thick exponential disk with an arctan rotation curve of $v(R) \propto v_{max} \arctan(R/R_t)$, where v_{max} is the maximum circular velocity and R_t is the turnover radius. A model galaxy consists of ten free parameters: centroid position (x, y), systematic velocity v_{sys}, line flux $S\Delta v$, half-light radius $R_{1/2}$, turnover radius R_t, inclination i, position angle PA, maximum circular velocity v_{max} and velocity dispersion σ_0. These parameters are convolved with the clean beam and are fitted to the data cube using a Markov chain Monte Carlo (MCMC) algorithm. The CO spectra extracted along

the kinematic major axis in the observed cube together with the best-fitting model are shown in Extended Data Fig. 3. The observed CO kinematics is well characterized by a rotating disk. The best-fit values are $Sd\nu = 1.88_{+0.02-0.01}$ Jy km s^{-1}, $R_{1/2} = 1.05 \pm 0.02$ kpc, $R_t = 0.18 \pm 0.03$ kpc, $i = 44° \pm 1°$, PA $= -64° \pm 1°$, $v_{max} = 227^{+5}_{-6}$ km s^{-1} and $\sigma_0 = 74 \pm 1$ km s^{-1}. We adopt the median and the 95% confidence interval of the last 60% of the MCMC chain for 20,000 iterations as the best-fit values and the uncertainties (Extended Data Fig. 4). For a symmetric oblate disk, the inclination corresponds to the projected minor-to-major-axis ratio of $q_{obs} = 0.73$ as $\sin^2(i) = (1-q^2_{obs})/(1-q^2_{int})$, assuming a disk thickness of[55] $q_{int} = 0.15$.

Toomre *Q* parameter. In a thin rotating gas disk with epicyclic frequency κ, the dispersion relation for an axisymmetric perturbation is $\omega^2 = \kappa^2 - 2\pi G\Sigma_{gas}|k| + \sigma^2_{0,gas}k^2$, where ω is the growth rate and k is the wavenumber of the perturbation[56–58]. The perturbation grows exponentially in time when $\omega^2 < 0$, leading to gravitational collapse of gas clouds. This condition is characterized by the Toomre Q parameter $Q = \kappa\sigma_{0,gas}/(\pi G\Sigma_{gas})$, and the threshold value is $Q_{cri} = 1$ for a thin gas disk and $Q_{cri} = 0.67$ for a thick disk[21,26]. When the disk consists of two components (gas and stars) with the same velocity dispersion, the threshold value increases to[59] $Q_{cri,2com} = 1.3$. The self-gravity of gas overcomes the repelling forces by pressure and differential rotation when $Q < Q_{cri}$. Using the maximum circular velocity derived from the disk model and the measured molecular gas mass per unit area and velocity dispersion without correction for beam-smearing, we estimated the local Q parameter in each pixel assuming a flat rotation curve with[58] $\kappa = 1.4v_{max}/R$ (Fig. 2). In Fig. 3, we show radially averaged CO fluxes and Q parameters along elliptical rings with the axis ratio of 0.73 using the best-fit kinematic parameters with correction for beam smearing and inclination.

Code availability. The ALMA data were reduced using the CASA pipeline version 5.1.1, available at https://casa.nrao.edu/casa_obtaining.shtml. The disk modelling code GalPaK^{3D} is publicly available at http://galpak.irap.omp.eu55.

Data availability. This work makes use of the following ALMA data: ADS/JAO. ALMA#2017.1.00300.S and 2017.A.00032.S. Calibrated data that support the findings of this study are publicly available in the ALMA archive (https://almascience.eso.org/aq/?project_code=2017.1.00300.S, https://almascience.eso.org/aq/?project_code=2017.A.00032.S). The HerMES data were obtained through the Herschel Database in Marseille (HeDaM; http://hedam.lam.fr), which is operated by CeSAM and hosted by the Laboratoire d'Astrophysique de Marseille.

31. Scott, K. B. et al. AzTEC millimetre survey of the COSMOS field – I. Data reduction and source catalogue. *Mon. Not. R. Astron. Soc.* **385**, 2225–2238 (2008).
32. Yun, M. S. et al. Early science with the Large Millimeter Telescope: CO and [C II] emission in the $z = 4.3$ AzTEC J095942.9+022938 (COSMOS AzTEC-1). *Mon. Not. R. Astron. Soc.* **454**, 3485–3499 (2015).
33. Toft, S. et al. Submillimeter galaxies as progenitors of compact quiescent galaxies. *Astrophys. J.* **782**, 68 (2014).
34. Chabrier, G. The galactic disk mass function: reconciliation of the Hubble Space Telescope and nearby determinations. *Astrophys. J.* **586**, L133–L136 (2003).
35. McMullin, J. P., Waters, B., Schiebel, D., Young, W. & Golap, K. CASA architecture and applications. *ASP Conf. Ser.* **376**, 127–130 (2007).
36. Smolčić, V. et al. The redshift and nature of AzTEC/COSMOS 1: a starburst galaxy at $z = 4.6$. *Astrophys. J.* **731**, L27 (2011).
37. Laigle, C. et al. The COSMOS2015 catalog: exploring the $1 < z < 6$ universe with half a million galaxies. *Astrophys. J. Suppl. Ser.* **24**, 224 (2016).
38. Roseboom, I. G. et al. The Herschel multi-tiered extragalactic survey: SPIRE-mm photometric redshifts. *Mon. Not. R. Astron. Soc.* **419**, 2758–2773 (2012).
39. Oliver, S. J. et al. The Herschel multi-tiered extragalactic survey: HerMES. *Mon. Not. R. Astron. Soc.* **424**, 1614–1635 (2012).
40. Smolčić, V. et al. The VLA-COSMOS 3 GHz large project: continuum data and source catalog release. *Astron. Astrophys.* **602**, A1 (2017).
41. da Cunha, E., Charlot, S. & Elbaz, D. A simple model to interpret the ultraviolet, optical and infrared emission from galaxies. *Mon. Not. R. Astron. Soc.* **388**, 1595–1617 (2008).
42. da Cunha, E. et al. An ALMA survey of sub-millimeter galaxies in the extended Chandra deep field south: physical properties derived from ultraviolet-to-radio modeling. *Astrophys. J.* **806**, 110 (2015).
43. Bruzual, G. & Charlot, S. Stellar population synthesis at the resolution of 2003. *Mon. Not. R. Astron. Soc.* **344**, 1000–1028 (2003).
44. Papadopoulos, P. P., Thi, W.-F. & Viti, S. C I lines as tracers of molecular gas, and their prospects at high redshifts. *Mon. Not. R. Astron. Soc.* **351**, 147–160 (2004).
45. Weiß, A. et al. Gas and dust in the Cloverleaf quasar at redshift 2.5. *Astron. Astrophys.* **409**, L41–L45 (2003).
46. Weiß, A. et al. Atomic carbon at redshift ~2.5. *Astron. Astrophys.* **429**, L25–L28 (2005).
47. Danielson, A. L. R. et al. The properties of the interstellar medium within a star-forming galaxy at $z = 2.3$. *Mon. Not. R. Astron. Soc.* **410**, 1687–1702 (2011).
48. Bothwell, M. S. et al. ALMA observations of atomic carbon in $z \sim 4$ dusty star-forming galaxies. *Mon. Not. R. Astron. Soc.* **466**, 2825–2841 (2017).
49. White, G. J. et al. CO and C I maps of the starburst galaxy M 82. *Astron. Astrophys.* **284**, L23–L26 (1994).
50. Wilson, C. et al. Luminous infrared galaxies with the submillimeter array. I. Survey overview and the central gas to dust ratio. *Astrophys. J. Suppl. Ser.* **178**, 189–224 (2008).
51. Bolatto, A. D., Wolfire, M. & Leroy, A. K. The CO-to-H_2 conversion factor. *Annu. Rev. Astron. Astrophys.* **51**, 207–268 (2013).
52. Downes, D. & Solomon, P. M. Rotating nuclear rings and extreme starbursts in ultraluminous galaxies. *Astrophys. J.* **507**, 615–654 (1998).
53. Carilli, C. L. & Walter, F. Cool gas in high-redshift galaxies. *Annu. Rev. Astron. Astrophys.* **51**, 105–161 (2013).
54. Bournaud, F. et al. Modeling CO emission from hydrodynamic simulations of nearby spirals, starbursting mergers, and high-redshift galaxies. *Astron. Astrophys.* **575**, A56 (2015).
55. Bouche, N. et al. GalPak3D: a Bayesian parametric tool for extracting morphokinematics of galaxies from 3D data. *Astrophys. J.* **150**, 92 (2015).
56. Toomre, A. On the gravitational stability of a disk of stars. *Astrophys. J.* **139**, 1217–1238 (1964).
57. Wang, B. et al. Gravitational instability and disk star formation. *Astrophys. J.* **427**, 759–769 (1994).
58. Binney, J. & Tremaine, S. *Galactic Dynamics* 2nd edn, 494–496 (Princeton Univ. Press, Princeton, 2008).
59. Romeo, A. B. & Wiegert, J. The effective stability parameter for two-component galactic discs: is $Q^{-1} \approx Q^{-1}_{stars} + Q^{-1}_{gas}$? *Mon. Not. R. Astron. Soc.* **416**, 1191–1196 (2011).

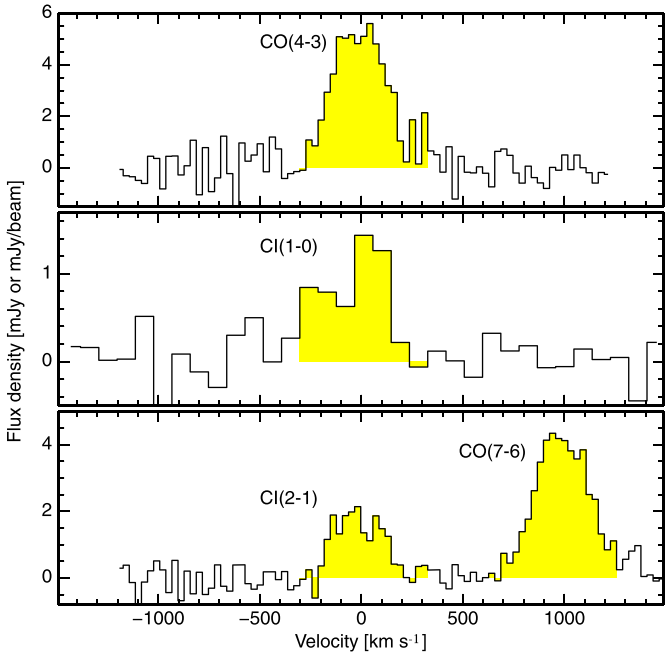

Extended Data Fig. 1 | Galaxy-integrated CO (4–3), CO (1–0) and C I (2–1) spectra of AzTEC-1. The CO (4–3) spectrum is extracted using an 0.8″-diameter aperture in the natural-weighted map cube. The C I (1–0) and C I (2–1) spectra are extracted from the peak positions in map cubes with 1.7″ × 1.1″ and 0.8″ × 0.7″ resolution, respectively. Yellow shaded regions show the velocity range $v = -315$ km s^{-1} to $v = +315$ km s^{-1}, in which the velocity-integrated line fluxes are measured.

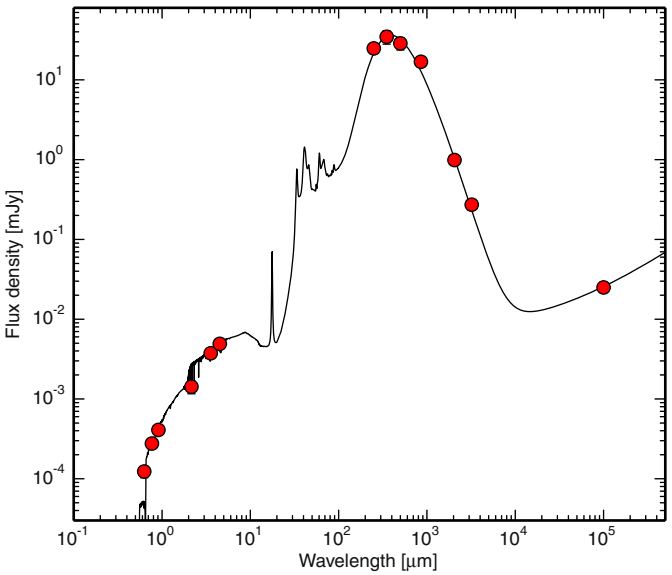

Extended Data Fig. 2 | Galaxy-integrated SED of AzTEC-1. Red circles show the photometric data from Subaru (r', i', z')[37], VISTA (K_s)[37], Spitzer (3.6 μm, 4.4 μm)[37], Herschel (250 μm, 350 μm, 500 μm)[38,39], ALMA (860 μm, 2.1 mm, 3.2 mm) and JVLA (10 cm)[40]. The black line shows the best-fitting SED model from MAGPHYS[41,42].

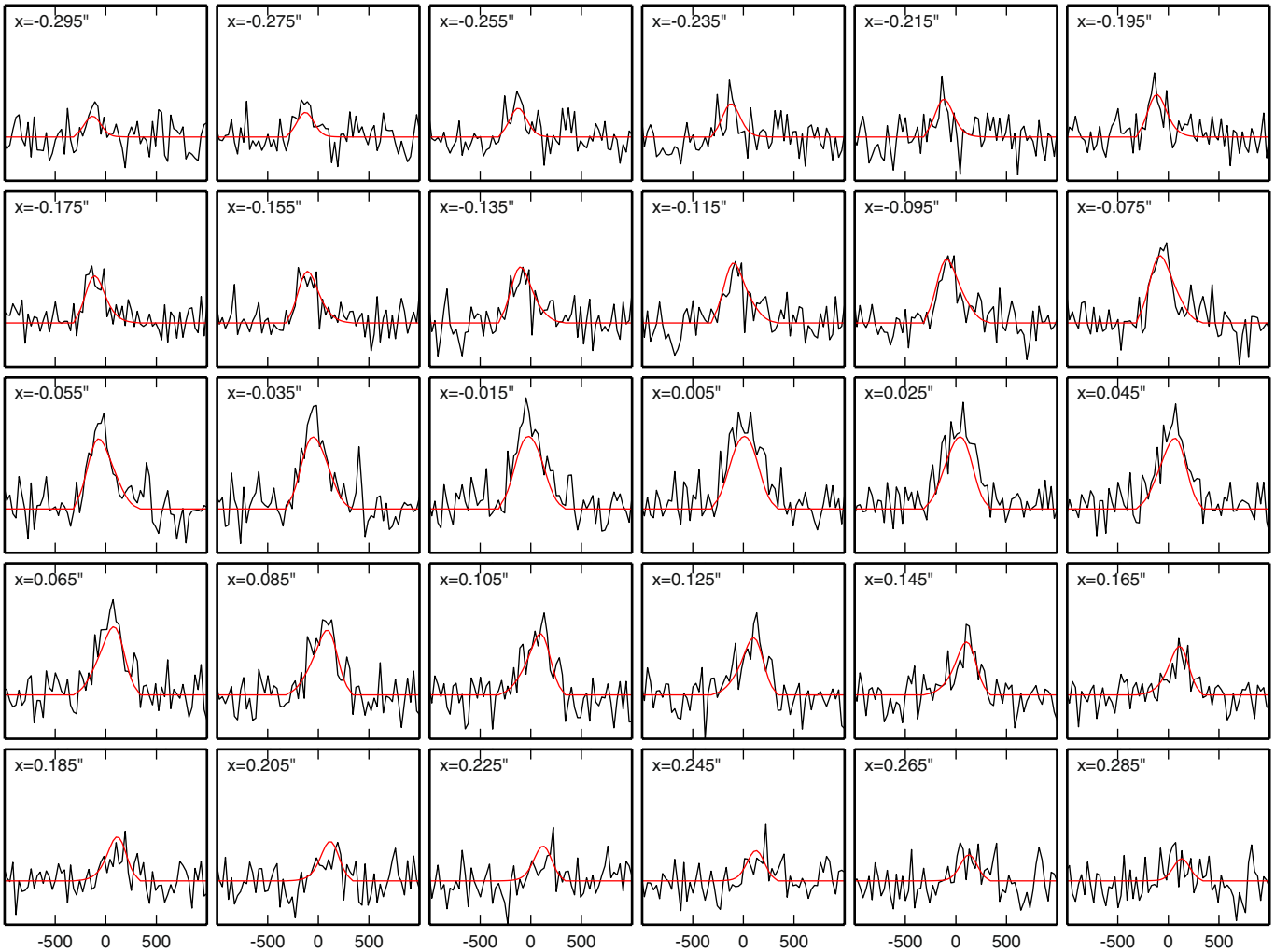

Extended Data Fig. 3 | CO spectra along the kinematic major axis. Spectra are extracted at a position angle of PA = −64°. The spatial offset *x* from the galactic centre is shown at the upper left of each panel. Red lines indicate the spectra of the best-fitting dynamical model produced by GalPaK^{3D}.

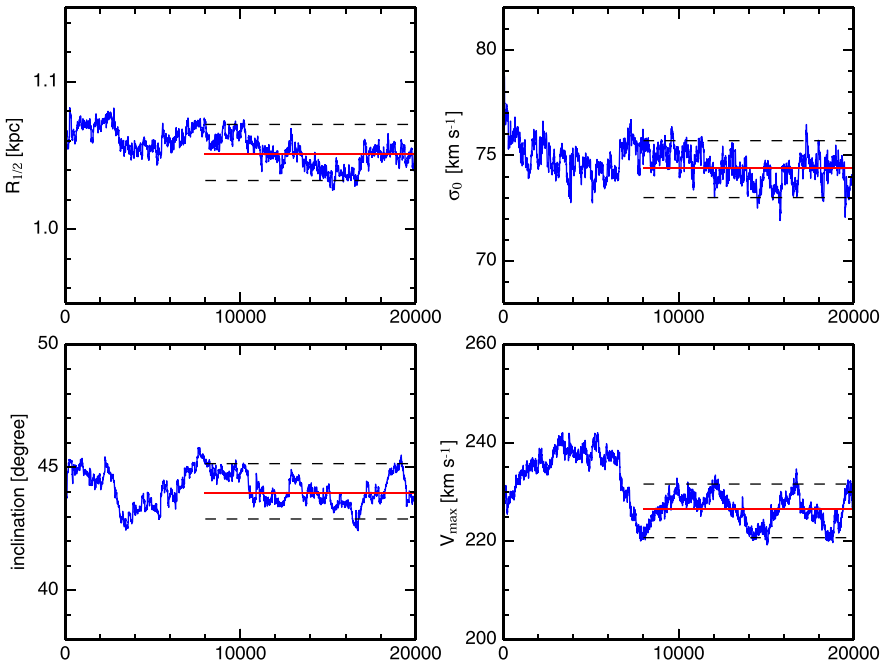

Extended Data Fig. 4 | Full MCMC chain for 20,000 iterations. Red solid lines and black dashed lines indicate the median and 95% confidence interval of the last 60% of the MCMC chain.

Extended Data Table 1 | Line fluxes in AzTEC-1

Line	Frequency (GHz)	$S_{\rm line}dv$ (Jy km s^{-1})	$L'_{\rm line}$ (10^{10}K km s^{-1} pc^2)
CO (4-3)	461.041	1.84±0.17*	8.21±0.78
CI (1-0)	492.161	0.45±0.08†	1.76±0.30
CI (2-1)	809.342	0.49±0.09‡	0.70±0.13
CI (2-1)	809.342	0.63±0.11†	0.92±0.16

*The flux within a 0.8″ aperture in the 0.093″ × 0.072″ map.
†The peak flux in the 1.7″ × 1.1″ map.
‡The peak flux in the 0.8″ × 0.7″ map.